

COMPARISON BETWEEN PATH LENGTHS TRAVELED BY SOLAR ELECTRONS AND IONS IN GROUND-LEVEL ENHANCEMENT EVENTS

LUN C. TAN^{1,2}, OLGA E. MALANDRAKI², DONALD V. REAMES³, CHEE K. NG⁴, LINGHUA WANG^{5,6},
IOANNA PATSOU², AND ATHANASIOS PAPAIOANNOU²

¹ Department of Astronomy, University of Maryland, College Park, MD 20742, USA; ltan@umd.edu

² Institute of Astronomy and Astrophysics, Space Applications and Remote Sensing, National Observatory of Athens, Athens, Greece

³ Institute for Physical Science and Technology, University of Maryland, College Park, MD 20742, USA

⁴ College of Science, George Mason University, Fairfax, VA 22030, USA

⁵ Department of Geophysics, Peking University, Beijing 100871, China

⁶ Space Science Laboratory, University of California, Berkeley, CA 94720, USA

Received 2012 September 4; accepted 2013 March 9; published 2013 April 16

ABSTRACT

We have examined the *Wind*/3DP/SST electron and *Wind*/EPACT/LEMT ion data to investigate the path length difference between solar electrons and ions in the ground-level enhancement (GLE) events in solar cycle 23. Assuming that the onset time of metric type II or decameter-hectometric (DH) type III radio bursts is the solar release time of non-relativistic electrons, we have found that within an error range of $\pm 10\%$ the deduced path length of low-energy (~ 27 keV) electrons from their release site near the Sun to the 1 AU observer is consistent with the ion path length deduced by Reames from the onset time analysis. In addition, the solar longitude distribution and IMF topology of the GLE events examined are in favor of the coronal mass ejection-driven shock acceleration origin of observed non-relativistic electrons. We have also found an increase of electron path lengths with increasing electron energies. The increasing rate of path lengths is correlated with the pitch angle distribution (PAD) of peak electron intensities locally measured, with a higher rate corresponding to a broader PAD. The correlation indicates that the path length enhancement is due to the interplanetary scattering experienced by first arriving electrons. The observed path length consistency implies that the maximum stable time of magnetic flux tubes, along which particles transport, could reach 4.8 hr.

Key words: acceleration of particles – Sun: coronal mass ejections (CMEs) – Sun: flares – Sun: particle emission – Sun: radio radiation

Online-only material: color figures

1. INTRODUCTION

1.1. Motivation of the Investigation

One of the fundamental questions in solar energetic particle (SEP) investigation is the acceleration mechanism of the highest energy (GeV and above) particles (Cliver 2008). Ions at these energies may interact in Earth’s atmosphere to produce secondary particles of sufficient intensity that can be detected by neutron monitors at ground level, causing the ground level enhancement (GLE) event. Since high-energy ions represent “hard” radiation that can be a significant hazard to astronauts and equipment in space, while secondary neutrons threaten passengers and crew of aircraft on polar routes, understanding where, when, and how particle acceleration takes place in the GLE event is also an important issue in space weather forecasting (Reames 2009a, 2009b). Taking into account typical ion energy spectra and the thickness of available shielding, the most important energy range of protons in space radiation damage is from 30 to 100–200 MeV (Turner 2006).

It is generally accepted that solar ions in GLE events are accelerated by the coronal mass ejection (CME)-driven shock waves, while the remnant suprathermal ions from previous SEP events may contribute to the seed population of shock-accelerated particles (Tylka & Lee 2006). The onset time analysis, which is based on the scatter-free transport assumption of first arriving particles, is often used to calculate the solar release time (SRT) and path length (L_0) that particles traveled from their release site near the Sun to the observer (e.g.,

Reames 2009a, 2009b). However, there has been a long-lasting divergence between L_0 values deduced from solar electron and ion data (e.g., Tylka et al. 2003; Mewaldt et al. 2003). The divergence might imply that the solar release site of electrons is different from that of ions. However, the divergence could be also due to particle transport effects; in particular, the transport of the first arriving electrons may not be scatter-free (see later Section 1.4.2). Recently, theoretical studies (Saiz et al. 2005; He et al. 2011; Rouillard et al. 2012) have shown the complexity of onset time analysis. Obviously, care should be taken to resolve the L_0 divergence between solar electrons and ions.

Without depending on the onset time analysis, Larson et al. (1997) and Kahler et al. (2011a, 2011b) calculated the L_0 value of electrons in the impulsive electron event occurring in a magnetic cloud (MC) by assuming that (1) these electrons are released at the onset time of type III radio bursts (RBs), (2) the interplanetary (IP) transport of first arriving electrons is scatter-free. Their approach provides a new way to decouple SRT deduction from the L_0 calculation, motivating us to adopt a similar way to estimate the L_0 value of solar electrons in the GLE event.

1.2. “Impulsive” Solar Particle Events

Small non-relativistic solar electron events appear to be the most common type of impulsive particle emission from the Sun (see the review of Lin 1985). Impulsive electron events were first observed at the electron energy $E_e > 40$ keV with a fast rise–slow decay time profile indicating the presence of significant particle

scattering in the interplanetary medium (IPM). Later, the events were detected down to $E_e \sim 1$ keV (and even $E_e \sim 0.1$ keV; see Gosling et al. 2003) with a fast rise–fast decay time profile indicating an essentially scatter-free propagation in the IPM (Lin 1974). In a few cases impulsive electron events are accompanied with impulsive ion events that exhibit higher ${}^3\text{He}/{}^4\text{He}$ and Fe/O ratios (so-called ${}^3\text{He}$ -rich event) and higher ionization status of Fe ions (Reames 1999).

Being different from the large “gradual” solar particle event that is attributed to the particle acceleration by CME-driven shocks, the impulsive particle event is linked to the reconnection-driven acceleration in solar flares. In particular, impulsive events are associated with intense fast-driving decameter-hectometric (DH) type III RBs, while gradual events are accompanied with slow-drifting metric type II RBs (see the review of Cliver 2008).

As an example of impulsive solar electron events, Wang et al. (2006) examined the 1999 August 7 event by using the *Wind*/3DP electron data of $E_e = 0.4\text{--}310$ keV. They noted that the observed time profiles of electron intensities at all energies fit well to triangular injections at the Sun with equal rise and fall times. At $E_e > 25$ keV the full width of half-maximum (FWHM) of injection electrons is <6 minutes. In addition, they found that at $E_e > 13$ keV the solar release time of electrons (SRT_e) is 7.6 ± 1.3 minutes later than the onset time (t_{III}) of type III RBs, whereas Krucker et al. (2007) observed a group of promptly arrived events with zero delay. Furthermore, by using the high-resolution interplanetary magnetic field (IMF) data from the *Wind* and *Advanced Composition Explorer* (ACE) spacecraft, Tan et al. (2011) examined the power spectral density (PSD) of the IMF in the 1999 August 7 event. Near and above the proton gyrofrequency they observed a steepening of PSD spectra due to the damping of electromagnetic ion cyclotron (EMIC) waves by solar-wind thermal ions. The steepening significantly reduces the PSD level above the proton gyrofrequency, preferring the occurrence of the scatter-free transport of low-energy electrons during a time period longer than 5 hr. Consequently, in the E_e range of 65–100 keV there appears to be an electron energy window, across which the scatter-free transport of lower energy electrons would change to the diffusive transport of higher energy electrons.

It is evident that through the open magnetic field lines involved in the reconnection process, solar particles accelerated in impulsive events may escape into the IPM and be detected by the 1 AU observer. Because of the small spatial extent of the reconnection region the involved field lines should be confined into a narrow ($\pm 20^\circ$) solar longitude cone centered at the well-connected longitude ($\sim \text{W}55^\circ\text{--}60^\circ$; see Reames 2002). Recently, observations from the *STEREO* and ACE spacecraft (Wiedenbeck et al. 2011) showed that an impulsive particle event can be seen over a large longitudinal angle of $\sim 136^\circ$. However, since the 2–4 MeV nucleon $^{-1}$ ${}^3\text{He}$ ions and 70–100 keV electrons observed at the poorly connected angle begin to arrive some ~ 16 and ~ 4 hr after the well connected onset, respectively, these particles should not be on the field lines directly connected to the flare. Instead, the large longitude spread of these particles could be due to slow processes, which need to be further studied. As pointed out by Wiedenbeck et al. (2011), “Observations of energetic particle flux “drop-outs” in rich SEP events (Mazur et al. 2000) have demonstrated that diffusive transport of energetic particles transverse to the heliospheric magnetic field is inefficient at distributing the particles in heliographic longitude. Thus, we discount this as a

possible mechanism for producing the large longitudinal spread that we observe.” In fact, the “drop-outs” of energetic particle intensities as observed by Mazur et al. (2000) and Chollet & Giacalone (2011) in the impulsive particle event have shown that the gap boundaries of arriving particles to be extremely sharp, indicating that these particles do not experience any significant cross-field transport. Reames (2013) hence suggested that the longitude spread of solar particles is due to a perpendicular transport process by which energetic particles must travel a long distance before finding a crossover point produced by the field-line random walk of Jokipii & Parker (1969). Note that the process is perpendicular transport, *not perpendicular diffusion*, because particles do not spread laterally at each radius. They only fill each flux tube, finding isolated crossover points at different radii to fill the next flux tube and eventually explore every nook and cranny of the field network. As a result, the particles from the impulsive particle events would be substantially delayed and attenuated when they spread to distant longitudes as observed by Wiedenbeck et al. (2011).

1.3. Current Status of Path Length Measurements of Solar Particles

Here we first mention the apparent inconsistency of L_0 measurements between Tylka et al. (2003) and Mewaldt et al. (2003). Tylka et al. (2003) carried out the onset time analysis of two large impulsive and three western GLE events by using the data of 100–300 keV electrons and ~ 2 MeV nucleon $^{-1}$ to ~ 2 GeV nucleon $^{-1}$ ions from *Wind*, ACE, and IMP-8, as well as available neutron monitors. They found that the onset time analysis of electrons matches that of ions, implying that $\text{SRT}_e \sim \text{SRT}_i$ and $L_{0e} \sim L_{0i}$. Hereafter, the subscripts e and i are used to denote electron and ion, respectively. In contrast, Mewaldt et al. (2003) examined 11 SEP events with enough intensity of the charge number $Z \geq 6$ ions by using 38–315 keV electron and 6–88 MeV nucleon $^{-1}$ ion data from the SIS and EPAM sensors on ACE, respectively. They found that only in four events, in which the 5–13 MeV nucleon $^{-1}$ ${}^3\text{He}/{}^4\text{He}$ ratio is >0.02 , do electrons and ions have similar SRT and L_0 values.

Compared with the onset time analysis of solar ions, the analysis of solar electrons displays more uncertainties. In the earlier works, SRT_e is deduced by assuming $L_{0e} \sim 1.2$ AU (Haggerty & Roelof 2002; Haggerty et al. 2003) or the length of the Parker spiral line under the observed solar wind speed (Krucker et al. 1999), which may result in errors. We hence mainly refer to Kahler & Ragot (2006), who carried out the onset time analysis of 80 near-relativistic solar electron events observed by *Wind*/3DP/SST. The L_{0e} values deduced from the electron velocity dispersion relation are broadly distributed between 0.15 and 2.7 AU. In most cases $L_{0e} < 1$ AU with a median value of 0.88 ± 0.09 AU, which is an unphysical result for the 1 AU observer. Also, they examined 23 separate *Wind*/3DP/EESA electron events at lower energies (down to $E_e \sim 1$ keV) and 24 combined SST+EESA events. For the separate EESA and combined SST+EESA events the median values of L_{0e} are 0.95 ± 0.07 AU and 0.99 ± 0.06 AU, respectively, which are higher than the L_{0e} value of SST events at higher energies.

In addition, during an MC event on 1995 October 18–20, Larson et al. (1997) observed five impulsive electron events. Assuming that solar electrons are released at the onset time of type III RBs (i.e., $\text{SRT}_e = t_{\text{RB}}$, where RB = III) they found that the $L_{0e\text{RB}}$ (i.e., $L_{0e\text{III}}$) value varies from ~ 3.2 AU near the

MC exterior to ~ 1.2 AU near the MC center. Nevertheless, no more impulsive electron events with $L_{0eIII} \geq 3.2$ AU have been observed since Larson et al. (1997), even though an extensive search for such event in MCs (Kahler et al. 2011b) and interplanetary coronal mass ejections (Kahler et al. 2011a) has been completed.

1.4. Possible Errors Involved in Electron Path Length Measurements

1.4.1. Lack of Deposition Energy Loss Correction of Wind/3DP/SST Electron Data

Since in the *Wind*/3DP/EESA-H data the instrumental noise mainly appears in the electron energy $E_e = 4\text{--}25$ keV range (Wang et al. 2006), we restrict ourselves to analyzing the *Wind*/3DP/SST electron data in the $E_e = 27\text{--}510$ keV range. Note that in the SST data $\sim 15\%$ of incident electrons scatter out of the silicon detector and leave only a fraction of E_e in it, producing an approximately even spectrum below E_e (Berger et al. 1969; Haggerty & Roelof 2002; Wang et al. 2011), which could imitate an earlier arrival of lower-energy electrons and produces a smaller L_{0e} value from the onset time analysis. Since the SST data downloaded from the 3DP Web site (<http://sprg.ssl.berkeley.edu/wind3dp/>) have not included the deposition energy loss correction, care should be taken when these data are used in the onset time analysis. As demonstrated below, the use of uncorrected SST data could result in an unphysical result of L_{0e} estimations. Therefore, in this work we have only used the SST data with deposition energy loss correction.

1.4.2. Interplanetary Transport of First Arriving Electrons May Not be Scatter-free

It is known (e.g., Reames 2009a, 2009b) that the onset time analysis of solar particles is based on the assumption that the particles that arrive first at the observer should experience scatter-free transport, with their pitch-angle (α) cosine value ($\mu = \cos(\alpha)$) of ~ 1 . This assumption sounds reasonable in the analysis of solar ion data, because in large SEP events the pre-event background level of ion intensity is usually low. The magnetohydrodynamic (MHD) waves that scatter ions are mostly self-excited (Ng et al. 2003). However, the situation may be different in the analysis of solar electrons. Because of the substantial presence of background electrons, usually both *R*-mode (whistler) and *L*-mode (EMIC) waves (Tan et al. 2011) that scatter non-relativistic electrons may already be amplified along the IP transport route of electrons. As a result, the IP transport of first arriving electrons may not be scatter-free.

In addition, in the SST measured E_e range (27–510 keV) Tan et al. (2011) observed the presence of an electron energy window, across which the electron scattering status would change from scatter-free at lower energies to diffusive at higher energies. While the location of the window is event-dependent, it is evident that in the E_e range of SST that the IP scattering of electrons should be increased with increasing E_e , which is different from the ion transport in which the IP scattering of ions is decreased with increasing ion rigidity (energy; Jokipii 1971). As a result, it is necessary to check the real scattering status, in particular for electrons at higher energies ($E_e > 65$ keV; see Tan et al. 2011, 2012).

Also, Tan et al. (2011) noted that the change of scattering status for higher energy electrons should occur in the local

environment (the heliocentric distance $r > 0.5$ AU) because of the dominant focused transport effect of SEPs at smaller r (see He & Wan 2012 and references therein). The notion of Tan et al. (2011) is consistent with that of Wang et al. (2011), who observed that in their examined impulsive electron events the time profiles of electron intensities retain a rapid-rise, rapid-decay peak and the estimated path length is only $\sim 4\text{--}18\%$ longer than the length of the Parker spiral line, indicating that electron scattering has indeed occurred near 1 AU. Therefore, the analysis of locally measured PAD of electrons could be helpful to understand the average scattering behavior of solar electrons along their entire IP transport route.

1.4.3. Temporal Variation of Magnetic Field Topologies

Because of the sampling time difference between electrons and ions there could be a “real” inconsistency between L_{0e} and L_{0i} if temporal variation of magnetic field topologies occurred during the examined event period. For example, Tan et al. (2012) observed that in the 2002 April 21 MC event the magnetic field topology seen by the *Wind* spacecraft during the first hour since the event onset is different from that during the later time, leading to $L_{0e} = 1.1 \pm 0.1$ AU being different from $L_{0i} = 1.49 \pm 0.05$ AU based on the onset time analysis. Therefore, care should be taken to check the temporal variation of magnetic field topologies during the examined event period.

1.5. Questions to be Addressed in This Work

Using solar ion data from *Wind*, IMP-8, *GOES*, and neutron monitors, based on the onset time analysis Reames (2009a) deduced the L_{0i} value of the GLE events during solar cycle 23, which provides a fiducial mark of ion path lengths to be compared with electron observations. We hence wish to calculate the L_{0e} value for those GLE events in order to compare it with the L_{0i} value deduced by Reames (2009a). However, before doing such comparison we need to answer a few questions.

1. What is the effect of deposition energy loss correction on *Wind*/3DP/SST electron data?

Since the deduction of L_{0e} is heavily dependent upon the quality of SST electron data, we need to compare the L_{0e} values deduced from the SST data with and without the deposition energy loss correction, in order to check whether or not the deposition energy loss corrected L_{0e} value could be consistent with the L_{0i} value deduced by Reames (2009a).

2. What type of RBs should be associated with the non-relativistic electrons observed in GLE events?

Since GLE events are characteristically linked with both big flares and fast CMEs, it is difficult to isolate the RB signatures associated with them (Cliver 2008). Therefore, in our further description we assume RB = II, although the replacement of RB = II by RB = III does not alter our conclusion. Later in Section 3, however, we will explain why additional observational evidences prefer RB = II.

3. What is the electron energy at which a valid electron path length can be deduced?

Since in Larson et al. (1997) and Kahler et al. (2011a, 2011b) L_{0e} is calculated at individual E_e channels of incident electrons, it is necessary to clarify at what E_e value the deduced L_{0e} value is valid. As mentioned above, Tan et al. (2011) noted that in the E_e range of SST the IP scattering of non-relativistic electrons would increase with

increasing E_e . Consequently, the L_{0eRB} value estimated at the lowest E_e value of SST should be close to the real value.

4. How can we accomplish the comparison between L_{0i} and L_{0eRB} ?

In order to compare L_{0i} with L_{0eRB} , the metric and D-H type II and III RB data as given in the Solar Geophysical Data (SGD) and by the *Wind*/WAVES instrument (Bougeret et al. 1995) are important. However, the RB data in SGD are often unreliable (Cane et al. 2010). Gopalswamy et al. (2012) wrote, “In some cases, discerning type II bursts from other emissions felt like an art rather than science.” Thus, they also examined the actual dynamic spectra from individual observatory Web sites (Hiraiso, Culgoora, IZMIRAN, Nancay), and from the Radio Solar Telescope Network (RSTN). In all cases, they were able to check the dynamic spectra and hence verify the onset times of metric type II RBs within a few minutes. Therefore, in order to enhance the reliability, our analysis includes the use of three independent sources of observations: L_{0i} data from Reames (2009a), RB data from Gopalswamy et al. (2012), and L_{0e} data from this work. As a result, to a maximum extent our analysis could avoid the lack of experiences in any branch of involved analysis works.

The comparison of thus deduced L_{0eRB} value with the L_{0i} value deduced by Reames (2009a) is presented in Section 2 and discussed in Section 3.

2. OBSERVATIONS

2.1. Observed Data

In this work, we use the *Wind*/3D Plasma and Energetic Particle Investigation (3DP; see Lin et al. 1995)/Semi-Conductor Detector Telescope (SST) electron data and the *Wind*/Energetic Particle Acceleration, Composition, and Transport Experiment (EPACT; see von Roseninge et al. 1995)/Low Energy Matrix Telescope (LEMT) heavy ion data. As explained above, the properties of RBs, flares, and CMEs for the GLE events during solar cycle 23 are taken from the compilation of Gopalswamy et al. (2012). Hereafter, the light-travel time of 8.3 minutes from the Sun to the Earth has been subtracted from the electromagnetic radiation observation time at 1 AU.

2.2. Effect of Deposition Energy Loss Correction for *Wind*/3DP/SST Electron Data

Based on the technique developed in Tan et al. (2009), we carry out the electron onset time analysis of the GLE events listed in Table 1 of Reames (2009a), using the uncorrected SST data that are directly downloaded from the 3DP Web site. In the onset time analysis, the observed time t of first arriving particles is plotted as a function of the particle velocity v ,

$$t = t_0 + L_0/v, \quad (1)$$

from which the solar release time (SRT = t_0) and the path length (L_0) traveled by first arriving particles from their release site near the Sun to the observer can be calculated. Among the 13 GLE events listed in Table 1 of Reames (2009a) there is a lack of SST data in the 2006 December 13 event. Also, we are not able to complete the analysis of the 2003 October 29 event because of the high intensity of background electrons coming from an earlier event.

For the remaining 11 GLE events based on the onset time analysis from the uncorrected SST electron data the deduced

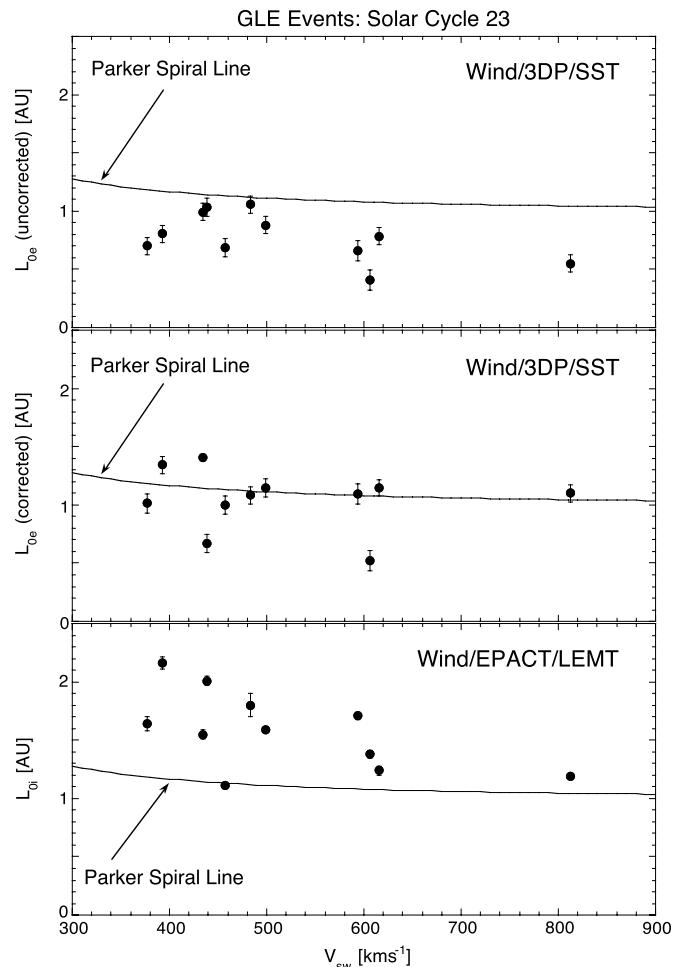


Figure 1. Particle path lengths deduced from the onset time analysis are shown as a function of the simultaneously measured solar wind speed (V_{sw}): the electron path length (L_{0e}) deduced from *Wind*/3DP/SST data without the deposition energy loss correction (top panel), L_{0e} deduced from the deposition-energy loss corrected SST data (middle panel), and the ion path length (L_{0i}) deduced by Reames (2009a; bottom panel).

path length L_{0e} is plotted versus V_{sw} in the top panel of Figure 1, where V_{sw} is the hourly averaged solar wind speed observed at the event onset and the solid line shows the length of the Parker spiral line at 1 AU as a function of V_{sw} . It can be seen that all L_{0e} data points are below the solid line, which is similar to Figure 4 of Kahler & Ragot (2006) displaying the SST data of the 80 solar electron events they examined. In fact, the median value of L_{0e} we deduced 0.79 ± 0.20 AU, which is consistent with 0.88 ± 0.09 AU deduced by Kahler & Ragot (2006), indicating that the lack of deposition energy loss correction of SST data may be the main reason causing an unphysical result of L_{0e} estimation.

Further, by using the deposition energy loss corrected SST data the re-calculated L_{0e} value is shown in the middle panel of Figure 1, where the data points are distributed around the Parker spiral line with the median value of $L_{0e} = 1.04 \pm 0.26$ AU. On the other hand, the ion path length L_{0i} deduced by Reames (2009a) is shown in the bottom panel of Figure 1, where the median value is $L_{0i} = 1.62 \pm 0.32$ AU. Therefore, the L_{0i} value deduced by Reames (2009a) is still inconsistent with the L_{0e} value deduced from the deposition energy loss corrected SST data.

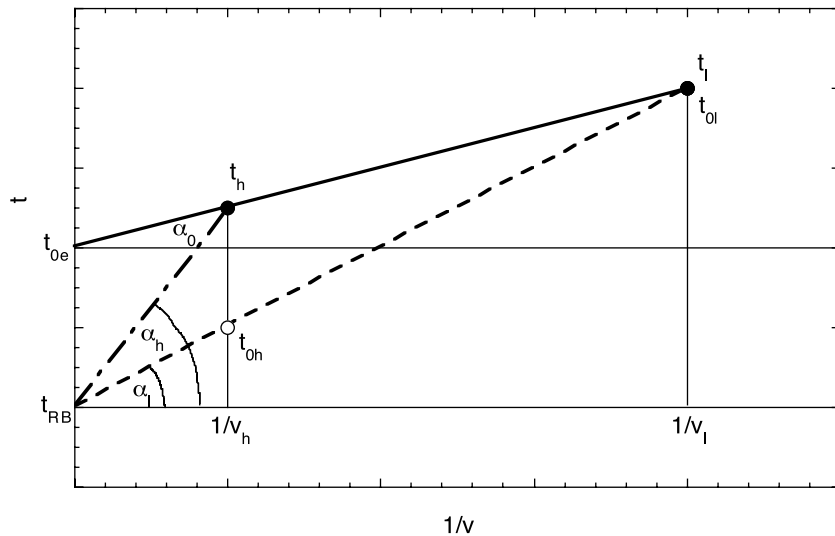


Figure 2. Calculation of electron path lengths is schematically described by plotting the electron arrival time t as a function of the reciprocal of electron velocity ($1/v$). The subscripts l and h denote the low-energy and high-energy points, respectively. SRT_e deduced from the onset time analysis and the onset time of radio bursts (RBs) are denoted by t_{0e} and t_{RB} , respectively.

2.3. Calculation of Electron Path Lengths by Assuming $SRT_e = t_{RB}$

2.3.1. Geometrical Explanation of L_{0eRB} Deduction

As mentioned in the Introduction, since in the SST measured energy range electron scattering increases with increasing E_e , only the IP transport of SST electrons at the lowest energy channel can be approximated to be scatter-free. Consequently, the valid L_{0eRB} value should be calculated at the lowest energy channel ($E_e \sim 27$ keV) of SST. As E_e increases the electron scattering status would change to become diffusive, resulting in a delay of their arrival time relative to the scatter-free transport time. That explains why the electron path length L_{eRB} deduced by Kahler et al. (2011b; see their Figure 3) is increased with increasing E_e (i.e., decreasing $1/v$).

Here we schematically describe the deduction process of both L_{0e} and L_{0eRB} in Figure 2, where the electron arrival time t is plotted versus the reciprocal of electron velocity ($1/v$) at the low-energy (l) and high-energy (h) points. In the figure the onset time analysis, which is based on the velocity dispersion relation, produces the solid line, whose slope ($\tan(\alpha_0)$) is equal to the path length L_{0e} . However, since in the SST energy range as E_e increases the electron scattering status would change from scatter-free at lower energies to diffusive at higher energies, only at the low-energy point the electron arrival time (t_l) can be approximated to the electron arrival time (t_{0l}) under the scatter-free transport assumption: $t_l \sim t_{0l}$. The slope of the dashed line ($=\tan(\alpha_l)$) is the path length (L_{0eRB}) traveled by low-energy electrons.

On the other hand, since at the high-energy point the first arriving electrons may not experience scatter-free transport, their arrival time t_h could be delayed relative to t_{0h} , the electron arrival time under the scatter-free transport assumption: $t_h > t_{0h}$. The path length (L_{eRB}) traveled by high-energy electrons is the slope ($\tan(\alpha_h)$) of the dot-dashed line. Since α_0 is less than α_l in Figure 2, we always have $L_{0e} < L_{0eRB}$. Also, since α_h is greater than α_l , L_{eRB} should increase with increasing E_e (or decreasing $1/v$; see Figure 3 in Kahler et al. 2011b).

For a given E_e value, from the first arrival time t of solar electrons we can calculate

$$L_{eRB} = v(t - t_{RB}), \quad (2)$$

where RB = II or III when the type II or type III RB is taken into account. Also, we have

$$L_{0eRB} = v_l(t_l - t_{RB}), \quad (3)$$

where the low-energy (l) point is at the lowest energy channel ($E_e \sim 27$ keV) of *Wind*/3DP/SST electrons. For the GLE events examined, our deduced L_{eRB} value at RB = II as a function of $1/v$ is shown in the upper panel of Figure 3. Similar to Kahler et al. (2011b), we also observe the increase of L_{eII} with decreasing $1/v$ (increasing E_e). In addition, among different GLE events the increasing rate of L_{eII} with E_e is different. In order to quantify the rate, we plot the deduced L_{eII}/L_{0eII} ratio as a function of $1/v$ in the lower panel of Figure 3, from which it can be seen that the 2001 April 18 and 2003 November 2 events have the highest rate, while the 1998 May 2 and 1998 May 6 events have the lowest rate. We will explain the rate difference in Section 2.4.

2.3.2. Comparison of L_{0eRB} with L_{0i}

Further, we assume that the estimated error of L_{0eRB} is the difference of L_{eRB} values between the two lowest adjacent E_e channels: $\Delta L_{0eRB} = L_{eRB}(\sim 40 \text{ keV}) - L_{eRB}(\sim 27 \text{ keV})$. For the GLE events examined the $L_{0eRB} \pm \Delta L_{0eRB}$ value thus deduced for RB = II is listed in Table 1 of this work.

Before doing the comparison between L_{0eRB} and L_{0i} , however, we need to check whether any significant time variation of magnetic field topologies occurred during the event period examined. By using the pitch angle spectrogram of SST electrons to perform such a check, we have observed one event (1998 August 24) in which the magnetic field topology exhibits significant variation. As shown in the upper panels of Figure 4, at the onset of the August event the electron injection is at $\mu \sim -1$, while during the later phase the injection is at $\mu \sim 1$. Because of the almost unchanged IMF direction, the μ change implies the change of IP transport routes of incident electrons during the event period. Also, in the lower panels of Figure 4 we show the time profiles of sectorized counting rate data of LEMT He ions. The rate data are the counts accumulated per 5 minutes in the two wide energy ranges (2.5–5 and 5–8 MeV nucleon⁻¹). Additional fluctuations of recorded counts can be seen in the rate data because of varying sampling time fractions for a given

Table 1
Solar Release Properties of the GLE Events in Solar Cycle 23

GLE	SRT _i ^a (UT)	L _{0i} ^a (AU)	SRT _e (UT)	L _{0e} (AU)	Flare Class/Location ^b	t _l (27 keV)	t _h (65 keV)	t _{II} ^b (UT)	t _{III} ^b (UT)	L _{0eII} (AU)	⟨μ _{omax} ⟩ (65 keV)	μ _{m,obs} (65 keV)
56	98 May 2 13:46.7	1.24 ± 0.04	13:31.6	1.15 ± 0.07	X1.1/S15W15	14:02.1	13:52.4	13:33	13:27	1.08 ± 0.07	0.79 ± 0.02	0.92 ± 0.09
57	98 May 6 08:03.5	1.11 ± 0.02	07:55.5	1.00 ± 0.08	X2.7/S11W65	08:21.3	08:13.5	07:55	07:53	1.01 ± 0.07	0.88 ± 0.02	0.94 ± 0.11
58	98 Aug 24 22:32.1	1.55 ± 0.04	22:18.8	1.41 ± 0.02	X1.0/N35E09	22:46.2	22:37.8	21:54	21:56	1.98 ± 0.11	0.42 ± 0.06	0.81 ± 0.05
59	00 Jul 14 10:16.5	1.71 ± 0.03	10:22.4	1.09 ± 0.09	X5.7/N22W07	10:51.6	10:42.9	10:11	10:10	1.54 ± 0.07	0.46 ± 0.02	0.86 ± 0.07
60	01 Apr 15 13:47.7	1.59 ± 0.01	13:51.1	1.15 ± 0.08	X14/S20W85	14:20.4	14:12.0	13:39	13:41	1.59 ± 0.13	0.52 ± 0.02	0.86 ± 0.07
61	01 Apr 18 02:24.3	1.80 ± 0.10	02:30.3	1.08 ± 0.07	—/S23W117	02:57.6	02:50.4	02:09	02:07	1.84 ± 0.26	0.50 ± 0.02	0.79 ± 0.05
63	01 Dec 26 05:20.6	1.64 ± 0.06	05:18.4	1.01 ± 0.08	M7.1/N08W54	05:48.6	05:39.0	05:04	05:05	1.69 ± 0.10	0.51 ± 0.03	0.86 ± 0.06
64	02 Aug 24 01:00.1	2.16 ± 0.05	01:09.3	1.34 ± 0.07	X3.1/S02W81	01:45.6	01:33.0	00:53	00:53	1.99 ± 0.07	0.59 ± 0.03	0.90 ± 0.06
65	03 Oct 28 11:05.1	1.38 ± 0.03	11:13.1	0.53 ± 0.09	X17/S20E02	11:27.0	11:22.8	10:54	10:55	1.24 ± 0.16	0.64 ± 0.05	0.76 ± 0.07
66	03 Oct 29 20:55.6	1.75 ± 0.09	N/A	N/A	X10/S19W09	N/A	N/A	20:34	20:33	N/A	N/A	N/A
67	03 Nov 2 17:13.8	2.01 ± 0.04	17:36.5	0.67 ± 0.08	X8.3/S18W59	17:55.8	17:47.4	17:06	17:08	1.91 ± 0.07	0.29 ± 0.03	0.82 ± 0.05
69	05 Jan 20 06:39.5	1.19 ± 0.02	06:39.6	0.96 ± 0.08	X7.1/N14W61	07:07.2	06:56.4	06:36	06:37	1.10 ± 0.07	0.65 ± 0.02	0.98 ± 0.12
70	06 Dec 13 02:34.0	1.72 ± 0.05	N/A	N/A	X3.4/S06W23	N/A	N/A	02:18	02:16	N/A	N/A	N/A

Notes. The light-travel time of 8.3 minutes from the Sun to the Earth has been subtracted from the electromagnetic radiation observation time at 1 AU.

^a From Reames (2009a).

^b From Gopalswamy et al. (2012).

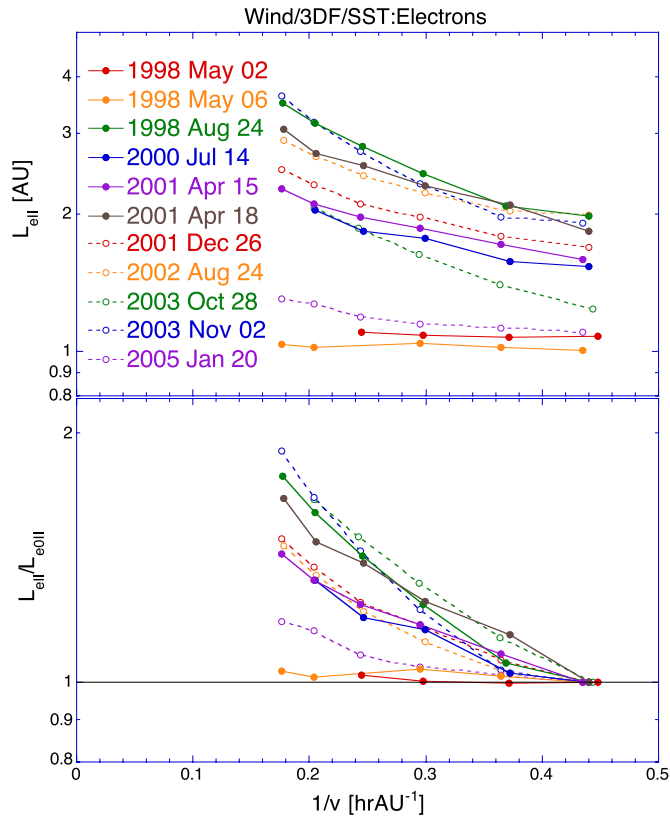


Figure 3. Assuming that the SRT_e of SST electrons is the onset time of type II RBs, for the GLE events in solar cycle 23 the deduced electron path length L_{eII} and the ratio of L_{eII} to L_{0eII} , the L_{eII} value given at the SST lowest energy channel ($E_e \sim 27$ keV), are plotted vs. $1/v$ in the upper and lower panels, respectively.

(A color version of this figure is available in the online journal.)

ion species in each 5 minute interval. Nevertheless, the rate data clearly exhibit that the first arriving He ions, which are delayed relative to the first arriving electrons, are at $\mu \sim 1$. Thus, both electron and He ion data consistently demonstrate the temporal variation of magnetic field topologies.

Therefore, the 1998 August 24 event (the open circle in Figure 5) should be rejected from the comparison between L_{0eRB}

and L_{0i} . For the remaining 10 GLE events (the solid dot) the comparisons between L_{0eII} and L_{0i} and between L_{0eIII} and L_{0i} are shown in the upper and lower panels in Figure 5, respectively. The least-squares fitting results are quite good, as the linear correlation coefficients between L_{0eRB} and L_{0i} are $R \sim 0.99$ in both RB = II and III cases, indicating that the probability, by which L_{0eRB} and L_{0i} are uncorrelated, is $P \sim 1 \times 10^{-7}$. However, from Figure 5 it is impossible to differentiate between RB = II and III because of the closeness of t_{II} and t_{III} . We hence calculate the weighted average of $L_{0eRB} = (0.91 \pm 0.04) L_{0i}$ for both RB = II and III, i.e., $L_{0eRB} \sim L_{0i}$ within an error range of $\pm 10\%$.

2.4. Correlation of L_{0eII} with Properties of Non-relativistic Solar Electron Events

2.4.1. Correlation of L_{0eII} with the Delay of Electron Arriving Times

A direct use of Figure 2 is to calculate the variation of L_{0eII} with the arriving time delay ($t_h - t_{II}$) of high-energy electrons. From Figure 2 we have

$$(t_l - t_{0e}) v_l = (t_h - t_{0e}) v_h. \quad (4)$$

Thus

$$\begin{aligned} L_{0eII} &= v_l(t_l - t_{II}) \\ &= v_l(t_h - t_{II}) + (v_h - v_l)(t_h - t_{0e}). \end{aligned} \quad (5)$$

Since $(v_h - v_l)(t_h - t_{0e})$ is a smaller quantity compared to $v_l(t_h - t_{II})$, we can approximate $(v_h - v_l)(t_h - t_{0e})$ as a constant, leading to a straight line plot of L_{0eII} versus $t_h - t_{II}$ with the slope and intercept being v_l and $(v_h - v_l)(t_h - t_{0e})$, respectively. The fitting result of $E_h \sim 65$ keV electrons is shown in the top panel of Figure 6, from which the linear correlation coefficient between L_{0eII} and $t_h - t_{II}$ is $R = 0.99$ ($P \sim 1 \times 10^{-7}$). The predicted slope ($v_l = 0.038$ AU min⁻¹) is consistent with the observed one (0.040 ± 0.002 AU min⁻¹). Also, from Table 1 of this work we find the averaged $\langle t_h - t_{0e} \rangle = 0.31 \pm 0.07$ hr for the GLE events examined, and thus the predicted intercept ($(v_h - v_l)(t_h - t_{0e})$) is 0.33 ± 0.07 AU, which is consistent with the observed value (0.27 ± 0.08 AU). It appears that the geometric explanation reproduces the IP transport of solar electrons in the GLE event well.

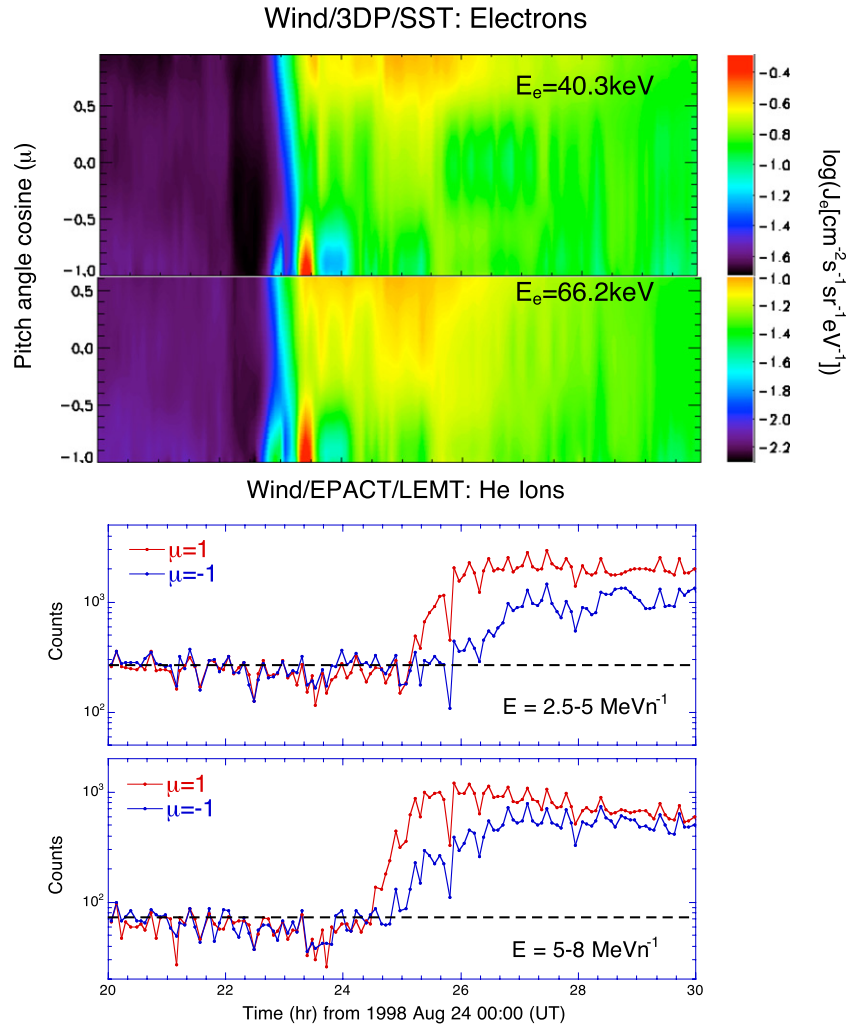


Figure 4. In the 1998 August 24 GLE event the pitch angle spectrograms of SST $E_e \sim 40$ and ~ 65 keV electrons with a 5 minute time resolution are shown in the upper panels. Also, the time profiles of sectorized counting rate data of LEMT He ions are plotted in the lower panels. The rate data are the counts accumulated per 5 minutes in the two wide E_e ranges (2.5–5 and 5–8 MeV nucleon $^{-1}$), in which additional fluctuations of recorded counts can be seen because of varying sampling time fractions for a given ion species.

(A color version of this figure is available in the online journal.)

2.4.2. Scattering Status of First Arriving Non-relativistic Electrons

As mentioned in Section 2.3.2, the 2001 April 18 and 2003 November 2 events have the highest increasing rate of L_{eII}/L_{0eII} with increasing E_e , while the 1998 May 2 and 1998 May 6 events have the lowest rate. What causes the rate difference?

In Tan et al. (2011) we defined the logarithmic increasing rate of the directional electron intensity (J_e) with increasing the pitch angle cosine (μ) of electrons,

$$\alpha_{PAD} = d \ln(J_e) / d\mu. \quad (6)$$

It is noticeable that α_{PAD} is a parameter characteristic of electron scattering status, because in the spherically symmetric radial diffusion model (Parker 1963) $\alpha_{PAD} > 3$ and < 1.5 as deduced from the peak intensity data of particles indicate the scatter-free and diffusive transport statuses of particles, respectively (see Tan et al. 2011). While the GLE events examined may not fit the model of Parker (1963) exactly, α_{PAD} is still a useful parameter to monitor the variation of electron scattering status.

We hence plot the time profile of α_{PAD} for the four extreme rate events in Figure 7, where the two lower energy channels

($E_e \sim 27$ and 40 keV) often exhibit a slower rise of lower α_{PAD} values, which is due to the presence of background electrons. Since background electrons usually have softer energy spectra and more isotropic PADs, their presence would result in a slower increase of smaller α_{PAD} values at lower E_e channels. Therefore, the maximum value of α_{PAD} at $E_e \sim 65$ keV as observed at $t_{\alpha PAD MAX}$ (the solid green line in Figure 7) will be used to characterize the electron scattering status at the event onset.

In Figure 7, it appears that in the 2001 April 18 and 2003 November 2 events the maximum value of α_{PAD} (~ 65 keV) is significantly lower than that in the 1998 May 2 and 1998 May 6 events, indicating that the increasing rate of L_{eII}/L_{0eII} ratios with increasing E_e is correlated to the increase of electron scattering.

Further, from Figure 7 it can be seen that the occurrence time of α_{PAD} maximum is delayed relative to the arrival time t_h (the green dot-dashed line). In order to explore the nature of such delay, we plot $t_{\alpha PAD MAX} - t_{II}$ versus $t_h - t_{II}$ in the second panel of Figure 6, where the least-squares fitting result between $t_{\alpha PAD MAX} - t_{II}$ and $t_h - t_{II}$ is shown by the solid line. It can be seen that $t_{\alpha PAD MAX} - t_{II}$ is correlated with $t_h - t_{II}$ with the linear correlation coefficient, $R = 0.83$ ($P = 1.6 \times 10^{-3}$).

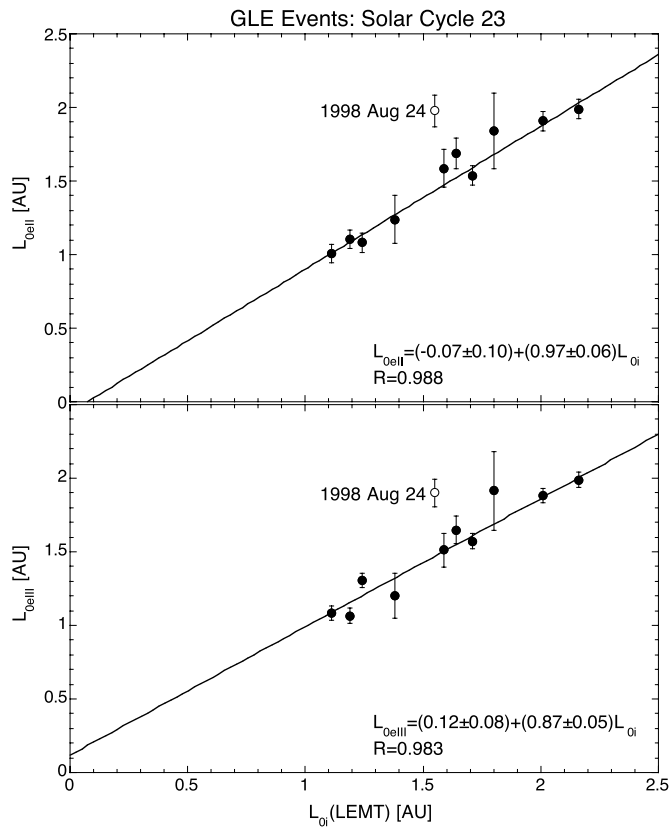


Figure 5. For the GLE events in solar cycle 23 the electron path lengths L_{0eII} (upper) and L_{0eIII} (lower) deduced under the assumption of $SRT_e = t_{RB}$, where $RB = II$ or III , are plotted vs. the ion path length L_{0i} deduced by Reames (2009a) from the onset time analysis. The 1998 August 24 event (the open circle) has been rejected from the comparison because of the occurrence of a significant change of magnetic field topologies during the event period.

In addition, by comparing the fitting line with the dashed line showing $t_{\alpha PADMAX} = t_h$, we find that the mean delay of $t_{\alpha PADMAX}$ relative to t_h is ~ 10 minutes. The delay is the time required for enhancing the α_{PAD} value characteristic of background electrons to that of first arriving incident electrons. In fact, assuming that at the event onset incident electrons have a step enhancement of α_{PADMAX} , we ought to observe a gradual increase of α_{PAD} before reaching α_{PADMAX} because of the “dilution” effect of background electrons. Therefore, the first arriving electrons should experience a scattering status characteristic of α_{PADMAX} . Since among the GLE events shown in Figure 7 their α_{PADMAX} values are different, the IP transport status of the first arriving $E_h \sim 65$ keV electrons may not be scatter-free.

2.4.3. What Affects the Increasing Rate of L_{eII}/L_{0eII} with Increasing E_e ?

According to Equation (5), from the deduced α_{PADMAX} value we can calculate the averaged μ value at α_{PADMAX} for first arriving $E_h \sim 65$ keV electrons,

$$\langle \mu_{\alpha PADMAX} \rangle = \int_{-1}^1 \mu \exp(\alpha_{PADMAX} \mu) d\mu \bigg/ \int_{-1}^1 \exp(\alpha_{PADMAX} \mu) d\mu, \quad (7)$$

whose value is listed in Table 1. The plot of $\langle \mu_{\alpha PADMAX} \rangle$ versus $t_h - t_{II}$ is shown in the third panel of Figure 6, which exhibits the tendency that $\langle \mu_{\alpha PADMAX} \rangle$ decreases with increasing $t_h - t_{II}$. The linear correlation coefficient between $\langle \mu_{\alpha PADMAX} \rangle$ and $t_h - t_{II}$ is $R = 0.84$ ($P = 1.2 \times 10^{-3}$). Therefore, from a joint analysis

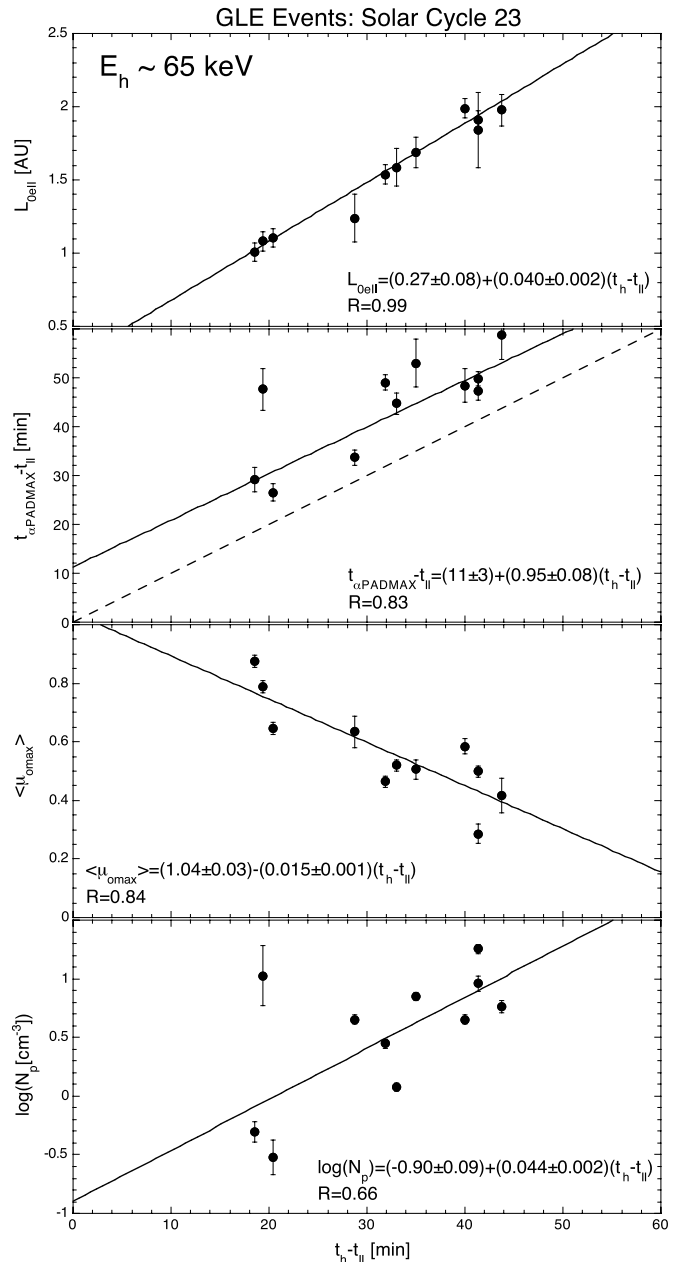


Figure 6. For $E_h \sim 65$ keV electrons in the GLE events of solar cycle 23 the deduced L_{0eII} value (top panel), the time difference $t_{\alpha PADMAX} - t_h$, where $t_{\alpha PADMAX}$ and t_h are the α_{PAD} maximum time of electrons and the onset time of type II RB, respectively (second panel), the mean μ value deduced from the locally measured α_{PAD} maximum, $\langle \mu_{\alpha PADMAX} \rangle$ (third panel), and the solar wind density (N_p) (bottom panel) are plotted vs. $t_h - t_{II}$, where t_h is the arriving time of $E_h \sim 65$ keV electrons.

of the top and third panels in Figure 6 we find that the GLE events with larger L_{0eII} values would have smaller $\langle \mu_{\alpha PADMAX} \rangle$ values, implying that due to stronger IP scattering the non-relativistic electrons in these GLE events should experience higher increasing rates of L_{eII}/L_{0eII} with increasing E_e .

Finally, in view of the observation by Cane (2003) and Kahler et al. (2007) that the delay of arrival times of near-relativistic electrons could be correlated with the locally measured solar wind density (N_p), we plot 1 hr averaged N_p data from the OMNI data set versus $t_h - t_{II}$ in the bottom panel of Figure 6, from which it can be seen that N_p and $t_h - t_{II}$ are indeed correlated with the linear correlation coefficient

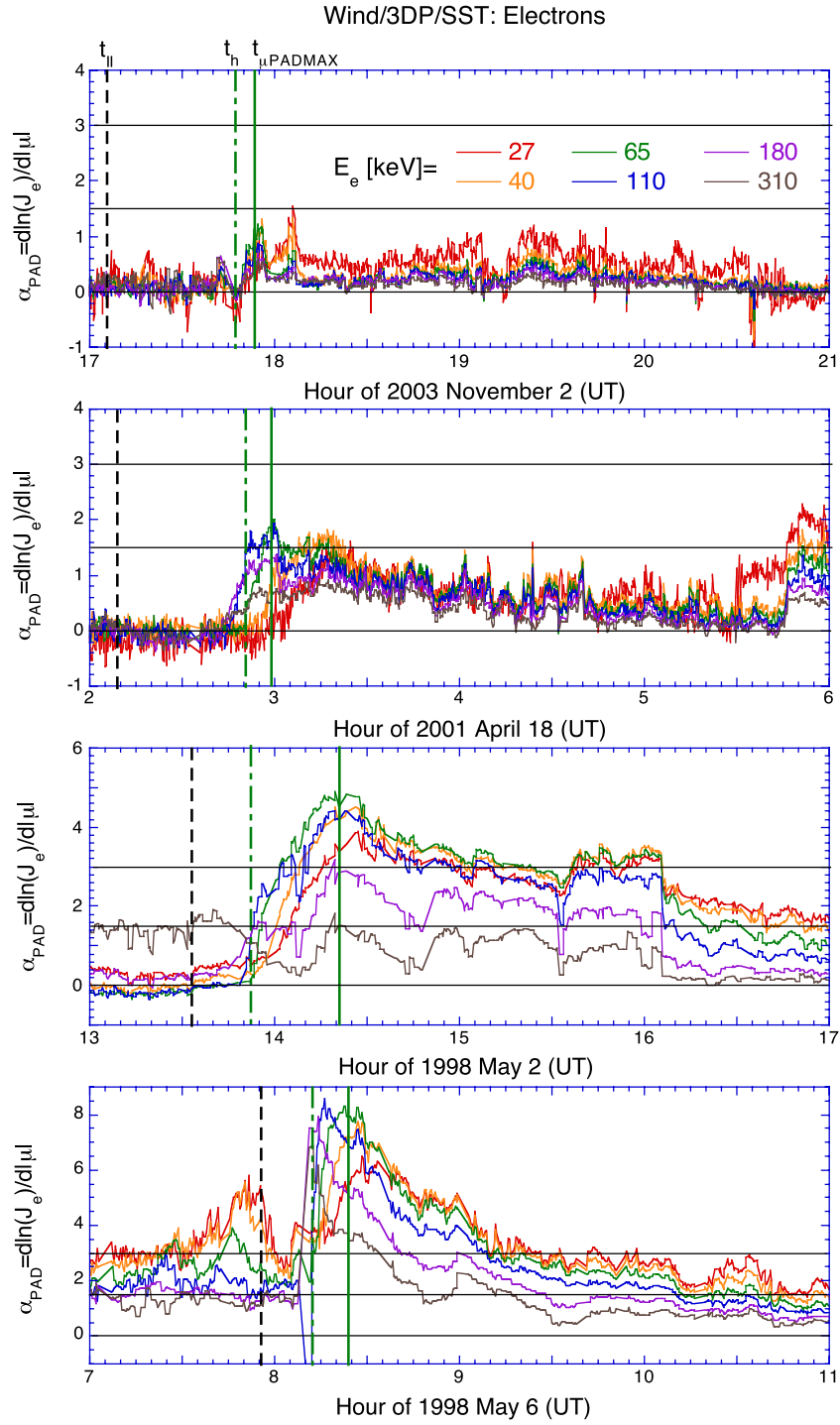


Figure 7. Time profiles of the pitch-angle-cosine increasing rate of directional electron intensity, α_{PAD} , for four GLE events, in which the rising rate of $L_{e\text{II}}/L_{0e\text{II}}$ with increasing E_e is significantly deflected from the average. The $\alpha_{\text{PAD}} = 1.5$ and 3.0 lines denote the upper and lower limits of the diffusive and scatter-free transport regions in the spherically symmetric radial diffusion model (Parker 1963), respectively.

(A color version of this figure is available in the online journal.)

$R = 0.66$ ($P = 2.7 \times 10^{-2}$) between $\log(N_p)$ and $t_h - t_{\text{II}}$. As explained in Section 2.3.1, the arrival time delay of $E_e \sim 65$ keV electrons is due to their IP scattering caused by the IMF turbulences in the local environment ($r > 0.5$ AU; see Tan et al. 2011; Wang et al. 2011). Since IMF turbulences are well correlated with the solar wind density fluctuations and the solar wind density itself is a reasonable proxy of its fluctuations (Richardson et al. 1998; Richardson & Paularena 2001), the correlation between N_p and $t_h - t_{\text{II}}$ is understandable.

2.4.4. Comparison of Locally Measured $\langle \mu_{\text{max}} \rangle$ with the μ Value Averaged Along the Entire Electron Path Length

As mentioned in Section 1, the change of electron scattering status should occur in the local environment because of the dominant focused transport effect of electrons at smaller r ($r < 0.5$ AU; Tan et al. 2011; Wang et al. 2011). The local nature of the change of electron scattering status is also seen from the correlation of the solar wind density locally measured with

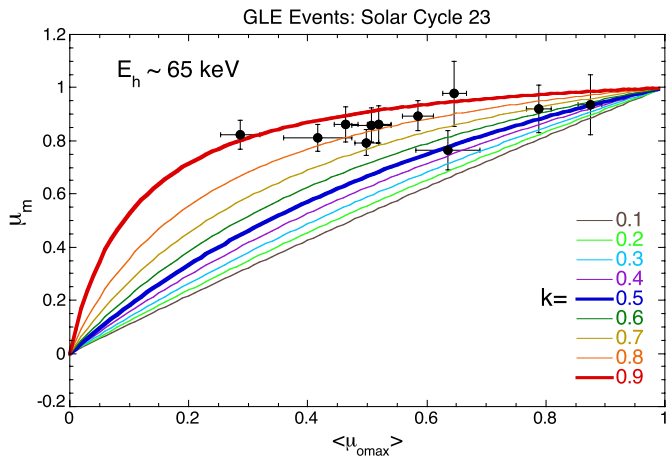


Figure 8. Mean μ value of $E_h \sim 65$ keV electrons deduced from the delay of electron arriving times relative to the scatter-free transport time ($\mu_{m,obs}$, the solid dots) is plotted vs. $\langle\mu_{omax}\rangle$. Also, the predicted μ_m values ($\mu_{m,pred}$), which are based on the assumption that the electron path length L_{0eII} can be divided into two parts comprising kL_{0eII} with $\mu = 1$ and $(1 - k)L_{0eII}$ with $\mu = \langle\mu_{omax}\rangle$ for different k values are shown by color lines.

(A color version of this figure is available in the online journal.)

the electron arrival time delay as described in Section 2.4.3. Therefore, incident electrons should keep their scatter-free transport status with $\mu \sim 1$ until $r \sim 0.5$ AU, beyond which the mean μ value of the first arriving electrons would change to $\langle\mu_{omax}\rangle$. In order to deduce the μ value (μ_m) averaged over $r = 0-1$ AU we divide the entire path length L_{0eII} into two parts comprising kL_{0eII} with $\mu = 1$ and $(1 - k)L_{0eII}$ with $\mu = \langle\mu_{omax}\rangle$ where $k < 1$. Thus μ_m should satisfy

$$t = t_0 + L_{0eII}/(\mu_m v), \quad (8)$$

where

$$L_{0eII}/(\mu_m v) = kL_{0eII}/v + (1 - k)L_{0eII}/(\langle\mu_{omax}\rangle v), \quad (9)$$

which results in the predicted μ_m value

$$\mu_{m,pred} = 1/(k(1 - 1/\langle\mu_{omax}\rangle) + 1/\langle\mu_{omax}\rangle). \quad (10)$$

On the other hand, assuming that in Figure 2 the change of arrival times of $E_h \sim 65$ keV electrons from t_{0h} to t_h is due to the change of their mean μ value from 1 to μ_m , we can deduce the observed μ_m value

$$\mu_{m,obs} = v_l(t_l - t_{II})/(v_h(t_h - t_{II})), \quad (11)$$

which is listed in Table 1 and plotted versus $\langle\mu_{omax}\rangle$ in Figure 8, where the color lines show the $\mu_{m,pred}$ values estimated at different k values. It can be seen that the $\mu_{m,obs}$ data are consistent with $k = 0.7 \pm 0.2$, which is again in support of our previous conclusion (Tan et al. 2011; Wang et al. 2011, Section 2.4.3) that the change of electron scattering status should occur in the local environment ($r > 0.5$ AU).

3. DISCUSSION

3.1. Analysis of Previous Observations

We first analyze the apparent inconsistency between the observations of Tylka et al. (2003) and Mewaldt et al. (2003) as mentioned in Section 1. It appears that the inconsistency is probably caused by the event selection criterion used in different

works. In fact, the two impulsive electron events selected by Tylka et al. (2003) should exhibit the scatter-free transport feature of the first arriving particles because of the fast rise–fast decay time profile of particle intensities observed (Lin 1974). Therefore, if the IP transport of non-relativistic electrons in the three GLE events selected by Tylka et al. (2003) is nearly scatter-free, we could expect that for all SEP events examined by Tylka et al. (2003) L_{0e} should be similar to L_{0i} .

Here we check the electron transport status in the three GLE events selected by Tylka et al. (2003). Among them two events are listed in Table 1 of this work, from which it can be seen that the 1998 May 6 and 2001 April 15 events have $\mu_{m,obs} = 0.94 \pm 0.11$ and 0.86 ± 0.07 , respectively, indicating that electron transport in these events is indeed close to scatter-free.

On the other hand, Mewaldt et al. (2003) classified the SEP events examined according to their ${}^3\text{He}/{}^4\text{He}$ ratios. There are four events with ${}^3\text{He}/{}^4\text{He} > 0.02$ and seven events with ${}^3\text{He}/{}^4\text{He} < 0.02$. Further, among the four ${}^3\text{He}/{}^4\text{He} > 0.02$ events, at least three belong to the impulsive particle events (Mewaldt et al. 2003), in which near-relativistic electrons should experience scatter-free transport (Lin 1974). In addition, from Figure 3 of this work it can be seen that in the fourth (1998 May 6) event non-relativistic electrons should also experience the scatter-free transport. Thus, the L_{0e} and L_{0i} values deduced from the onset time analysis could be close to each other in all four ${}^3\text{He}/{}^4\text{He} > 0.02$ events selected by Mewaldt et al. (2003).

Thus, the apparent inconsistency between Tylka et al. (2003) and Mewaldt et al. (2003) can be reduced to a notion that in the seven ${}^3\text{He}/{}^4\text{He} < 0.02$ events selected by Mewaldt et al. (2003) electron transport should not be scatter-free, which sounds reasonable because of the diffusive transport feature of SEPs in these gradual SEP events (Tan et al. 2011).

Furthermore, we note that Tylka et al. (2003) only used the SST electron data at $E_e > 100$ keV, which could be due to the fact that the use of SST electron data without deposition energy loss correction would imitate an earlier arrival of lower-energy electrons as described in Section 1. Also, the $L_{0e} < 1$ AU observed by Kahler & Ragot (2006; see Section 3.1) could be due to the same reason. However, the difference of median L_{0e} values between EESA-H (down to ~ 1 keV) and SST (> 25 keV) data as observed by Kahler & Ragot (2006) is probably caused by the change of electron scattering status with increasing E_e (Tan et al. 2011). Since in the EESA-H events the velocity dispersion plot of electron arrival times is weighted by electron data at lower energies, where electron scattering is closer to being scatter-free, a less distorted or higher L_{0e} value should be found from EESA-H data.

3.2. Implication of Our Observations

Since the correlation analysis shown in Figure 5 cannot differentiate between $\text{SRT}_e = t_{II}$ and $\text{SRT}_e = t_{III}$ because of the closeness of t_{II} and t_{III} , we turn to the longitude distribution of solar flares that are associated with the GLE events examined. As described in Section 1.2, solar particles accelerated in impulsive events should be confined into a narrow ($\pm 20^\circ$) solar longitude cone centered at the well-connected longitude ($\sim W55^\circ-60^\circ$). Indeed, the impulsive electron event is observed in the well-connected longitude range ($W30^\circ$ to $W90^\circ$; see Lin 1974; Kahler 2007), and the ${}^3\text{He}$ -rich ion event has a similar longitude distribution (Reames 1999; Nitta et al. 2006; Tylka et al. 2012). According to Reames (1999), the longitude distribution mainly results from the variation in solar-wind speed, while the random walk of field lines also plays a smaller role. Consequently, the

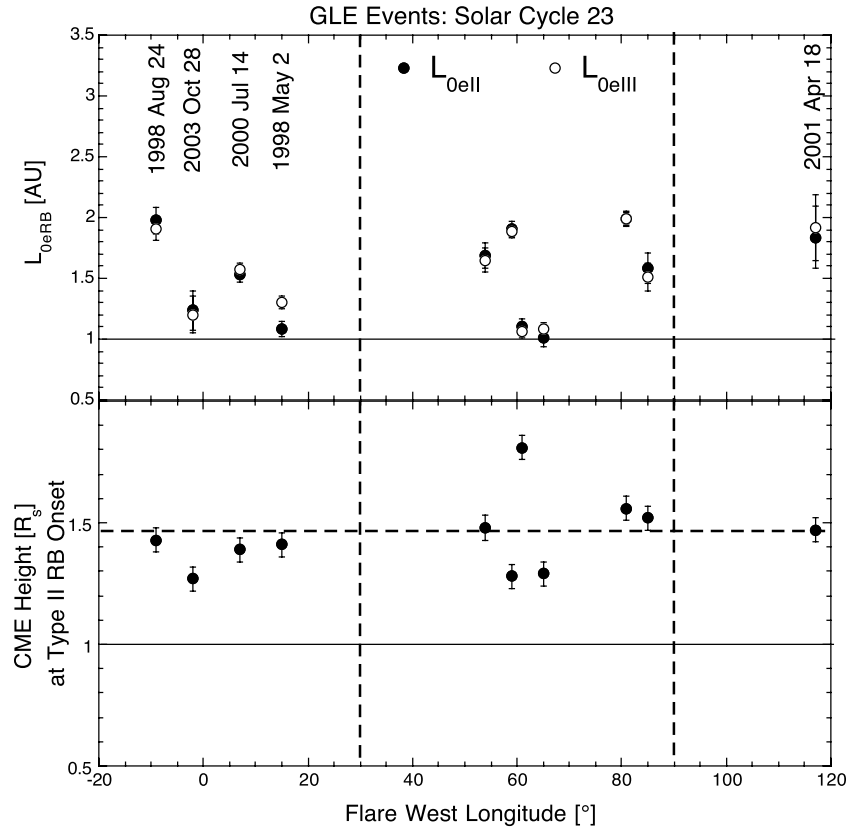


Figure 9. For the GLE events in solar cycle 23 the solar flare longitude distributions of L_{0eRB} and CME heights at the type II RB onset are shown in the upper and lower panels, respectively. The two vertical dashed lines limit the well-connected longitude range.

true cone of particle emission in the impulsive particle event should be smaller (Kahler et al. 2007).

The solar longitude distribution of the GLE events examined is shown in the upper panel of Figure 9, where the two vertical dashed lines limit the well-connected longitude range. What we are interested in are those GLE events outside the well-connected longitude range, where electrons emitted from the flare acceleration process should feel difficult to reach the 1 AU observer. We hence label these events in Figure 9. Surprisingly, we note that the 2003 October 28 (E02°) and 1998 May 2 (W15°) events have $L_{0eRB} \sim 1.2$ AU, which is the length of the Parker spiral line at 1 AU under the average solar wind speed (Figure 1), implying that the non-relativistic electrons in the two events should come from the well-connected longitude range.

We further examine the IMF data in order to explore the magnetic field topology involved in the two events. In Figure 10, the pitch angle spectrogram of *Wind*/3DP/SST $E_e \sim 40$ keV electrons and the time profile of the longitude (ϕ_B) and latitude (θ_B) of the IMF are shown in the upper and lower panels for the 1998 May 2 and 2003 October 28 events, respectively. Since a detailed analysis of the IMF topology in the May event was made in Tan et al. (2012), we first examine the magnetic field vector \mathbf{B} in the May event. It can be seen from Figure 10 that at the event onset \mathbf{B} is nearly Sunward with a large latitudinal component. Incident electrons are along the antisunward direction with $\mu \sim -1$, while reflected electrons are along the Sunward direction with $\mu > 0$. Here particle reflection is due to the magnetic mirroring effect formed in the bottleneck of magnetic field lines draped around the west flank of a preceding CME (Tan et al. 1992, 2009, 2012; Bieber et al. 2002). The observed Sunward \mathbf{B} with a large latitudinal component is consistent with the Parker spiral line distorted by the obstacle formed in the west flank of

a CME (see Figure 9 in Tan et al. 2009). In addition, Figure 10 shows that the IMF configuration in the October event is similar to that in the May event: \mathbf{B} is nearly Sunward with a large latitudinal component. The similarity implies a common origin of the field line distortion in the two events (although we do not observe the reflected electron beam in the October event). Therefore, the IMF observation is also consistent with incident electrons in the two events should come from the well-connected longitude range.

Since in the two events the event-associated flare is located at $\sim W0^\circ$, the cone of field lines that directly connect to flare particle emission must be restricted to a narrow longitude ($\pm W20^\circ$) range (Reames 2002). Thus, the electrons produced in the flare acceleration process cannot directly access the 1 AU observer. As explained in Section 1.2, in order to spread to distant longitudes the particles from the flare acceleration process must be delayed and attenuated as observed by Wiedenbeck et al. (2011), which is in conflict with the observed prompt arrival of electrons with $L_{0eRB} \sim 1.2$ AU.

Therefore, the solar longitude distribution and IMF topology of the GLE events examined are in favor of the CME-driven shock acceleration origin of non-relativistic electrons in the GLE events examined. Since our observations show that both non-relativistic electrons and energetic ions could originate from the same shock acceleration process, it is understandable why both particles would have closer path lengths when they travel from their release site near the Sun to the 1 AU observer. We then estimate the CME height at type II RB onsets. From Table 1 of Gopalswamy et al. (2012) the flare longitude distribution of CME heights at the type II RB onset for the GLE events examined is shown in the lower panel of Figure 9, from which the mean height is $1.5 \pm 0.2 R_s$ (R_s is the solar radius).

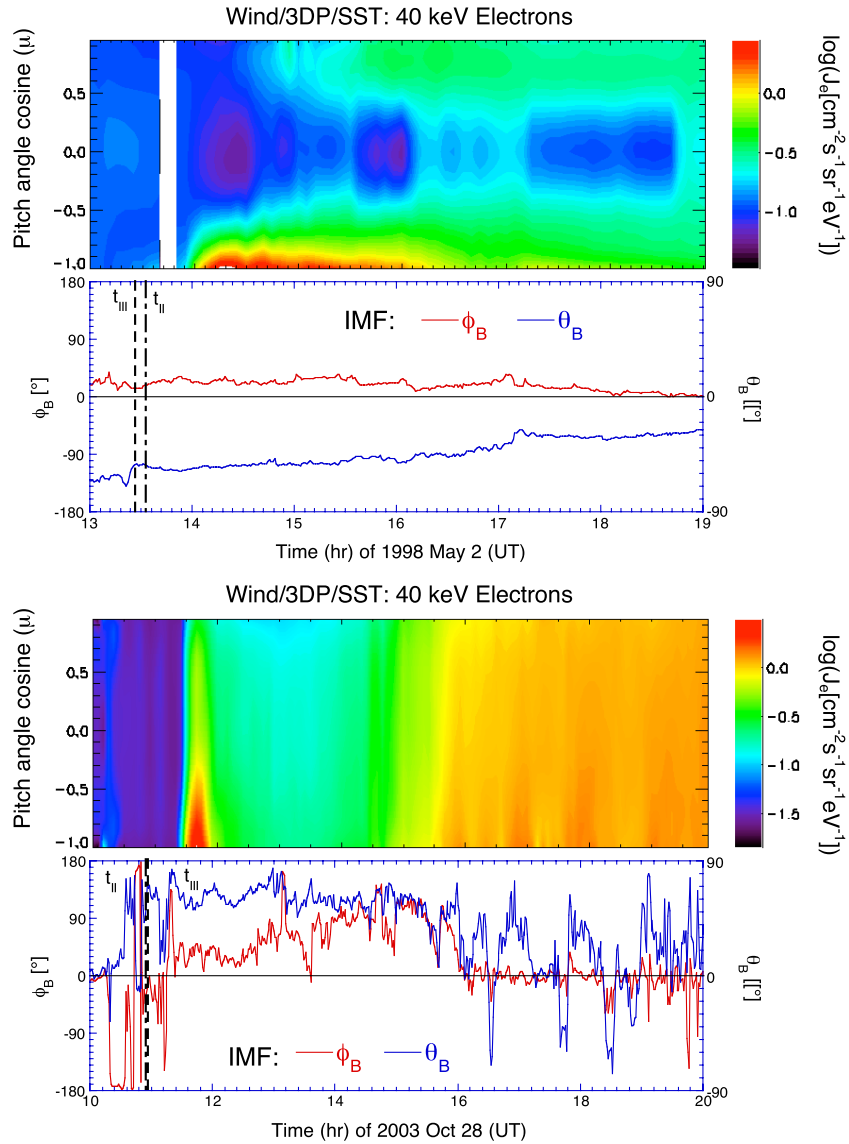


Figure 10. The pitch angle spectrogram of SST $E_e \sim 40$ keV electrons and the time profile of the longitude (ϕ_B) and latitude (θ_B) of the IMF are shown in the upper and lower panels for the 1998 May 2 and 2003 October 28 events, respectively.

(A color version of this figure is available in the online journal.)

Here we explain the main difference in the RB characteristics between the flare- and shock-accelerated SEP events (see the review of Reames 2013). Only along open field lines can solar electrons escape into the IPM to generate type III RBs, which are due to electron transport (Kundu 1965), independently of the acceleration source. Fast electrons streaming out ahead of slower ones would produce a “bump-on-tail” distribution function that is observed to produce Langmuir waves and subsequent radio emissions (see Thejappa et al. 2012; Graham et al. 2012, as well as the references therein). According to Wild et al. (1963), fast-driving type III RBs are the defining signature of particle acceleration by solar flares, because open field lines can be involved in the reconnection process of flare particle acceleration. On the contrary, in large gradual particle events like the GLE events examined, electrons originating from the reconnection-driven acceleration process would be trapped, because the magnetic reconnection occurs on closed field lines beneath the CME (Reames 2002).

Furthermore, CME-driven shock waves are manifested by slow-drifting type II RBs. Type II bursts are believed (see, e.g.,

Ganse et al. 2012) to be produced by electrons accelerated in the foreshock region of a shock front, where the field lines lie near the plane of the shock, perhaps even intersecting the shock surface in multiple locations. Electrons are accelerated as they drift in the electric field of a quasi-perpendicular shock. Counter-streaming electrons generate counter-streaming Langmuir waves that interact to produce the electromagnetic radiation observed as type II RBs. Since the field lines containing the electrons are soon swept downstream of the shock, the electrons may not escape. However, if they were able to find a path of outward escape, they could produce type III RBs. Shocks themselves do not produce type II RBs.

Since the spacecraft measurement of IMF cannot be used to verify the stability of magnetic flux tubes because of a small correlation scale length of the magnetic field (~ 0.008 AU; see Matthaeus et al. 2005), the velocity difference between faster electrons and slower ions provides a method to estimate the stability of magnetic flux tubes. Taking into account the maximum L_{0i} value found from the 2002 August 24 event (see Table 1) and the minimum energy of LEMT He ions

(~ 1.8 MeV nucleon $^{-1}$), the estimated maximum stable time is 4.8 hr.

3.3. Why Did Kahler et al. (2011a, 2011b) Not Observe Electron Path Lengths of > 3.2 AU?

Finally, we attempt to answer an interesting question: why did Kahler et al. (2011a, 2011b) not observe the electron path length of > 3.2 AU in the exterior region of MCs under the $SRT_e = t_{III}$ assumption? In fact, from Figure 6 of this work we note a tendency that GLE events with larger L_{0eII} values have smaller $\langle \mu_{0max} \rangle$ values, implying that non-relativistic electrons in these events should experience stronger IP scattering. Extrapolating the tendency to $L_{0eII} > 3$ AU, the $\langle \mu_{0max} \rangle$ value of ~ 65 keV electrons could be zero, indicating an isotropic PAD of electrons. Analysis (not shown here) exhibits that the variation tendency of L_{0eIII} is similar to that of L_{0eII} . Since under an isotropic PAD the diffusive transport of particles should no longer happen, in the exterior of MCs $E_e > 65$ keV electrons would not diffusively transport along the helically wound magnetic field line to reach the 1 AU observer. Instead, the frequent occurrence of interchange reconnections between the outer fields of MCs and the surrounding solar wind fields could provide direct magnetic connections between the Sun and the 1 AU observer as suggested by Kahler et al. (2011b).

Therefore, unless electron scattering is extremely weak we cannot use > 65 keV electrons to measure L_{0eIII} of > 3 AU under the $SRT_e = t_{III}$ assumption. In this sense, the 1995 October 18–20 MC event examined by Larson et al. (1997) is unusual, because in the event, electron scattering is negligible. This point can be confirmed by Figure 1 of Larson et al. (1997), also Figure 1 of Kahler et al. (2011b), which shows that the observed $L_{eIII} = 3.2$ AU is independent of E_e . Remember that (see Figure 3 of this work) an E_e -independent L_{eRB} implies that the electron transport is scatter-free over the entire E_e range. Thus, the valid result of $L_{eIII} = 3.2$ AU obtained by Larson et al. (1997) is guaranteed by a negligible electron scattering level over the entire E_e range examined.

However, it can be seen from Table 1 and Figure 3 of Kahler et al. (2011b) that in the rest of the MC events they examined electron scattering is not negligible as their deduced L_{eIII} values exhibit a significant increase with increasing E_e . Thus from the observed data at different E_e channels they deduced different L_{eIII} values for the same impulsive electron event. As a result, in their Table 1 only an L_{eIII} interval (L_e in the fifth column) is provided for each impulsive electron event. According to Figure 3 of this work the lower limit of the interval should be close to the L_{0eRB} value given in Section 2.3.1. For the only event common to Table 1 of Kahler et al. (2011b) and Table 1 of this work (the 1998 May 2 event) we note that the lower limit of the L_{eIII} interval (1.0 AU) given in Table 1 of Kahler et al. (2011b) is indeed close to the L_{0eII} (1.08 ± 0.07 AU) given in Table 1 of this work, although a detailed comparison cannot be carried out without taking into account the deposition energy loss correction (Section 2.2).

It seems that significant electron scattering found inside MC could be in conflict with the general view that inside MCs the magnetic turbulence is extremely weak. However, it should be emphasized that particle scattering near the MC boundary is significantly different from that in the MC interior region. In fact, Torsti et al. (2004) already noted that in the 1998 May 2 MC event near the MC boundary the first-order anisotropy of 17–22 MeV protons is close to zero (see their Figure 1), while the

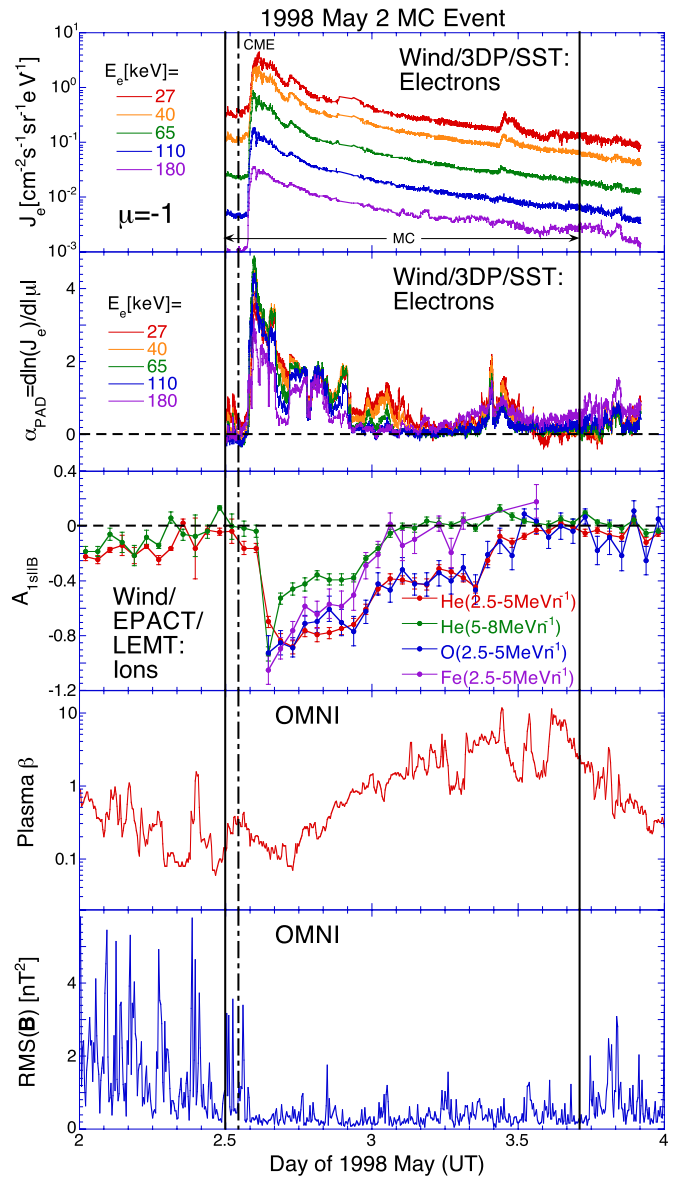


Figure 11. Time profiles of the incident electron intensity measured by SST, the α_{PAD} value deduced from SST electron data, the parallel to the \mathbf{B} component of the first-order anisotropy vector of LEMT heavy ions in the solar wind frame ($A_{||B}$), the plasma β value, and the root mean square deviation of the magnetic field vectors ($RMS(\mathbf{B})$) are shown from the top to bottom panels for the 1998 May 2 MC event, respectively.

(A color version of this figure is available in the online journal.)

magnitude of ion anisotropies is anti-correlated to the intensity of magnetic fluctuations whose spatial scale is comparable to the particle Larmor radius (Kocharov et al. 2007).

Here we further analyze the details of particle scattering in the exterior region of two MC events examined in Tan et al. (2012). For the 1998 May 2 and 2002 April 21 events the time profiles of the directional intensity of incident electrons streaming away from the Sun along the IMF direction as measured by SST, the α_{PAD} value deduced from SST data, the component parallel to \mathbf{B} of the first-order anisotropy vector of LEMT heavy ions in the solar wind frame ($A_{||B}$) (see Tan et al. 2007), as well as the plasma β (the ratio of the proton thermal energy to magnetic energy) and the root mean square deviation of magnetic field vectors ($RMS(\mathbf{B})$), both of which are from the OMNI dataset, are shown in Figures 11 and 12, respectively.

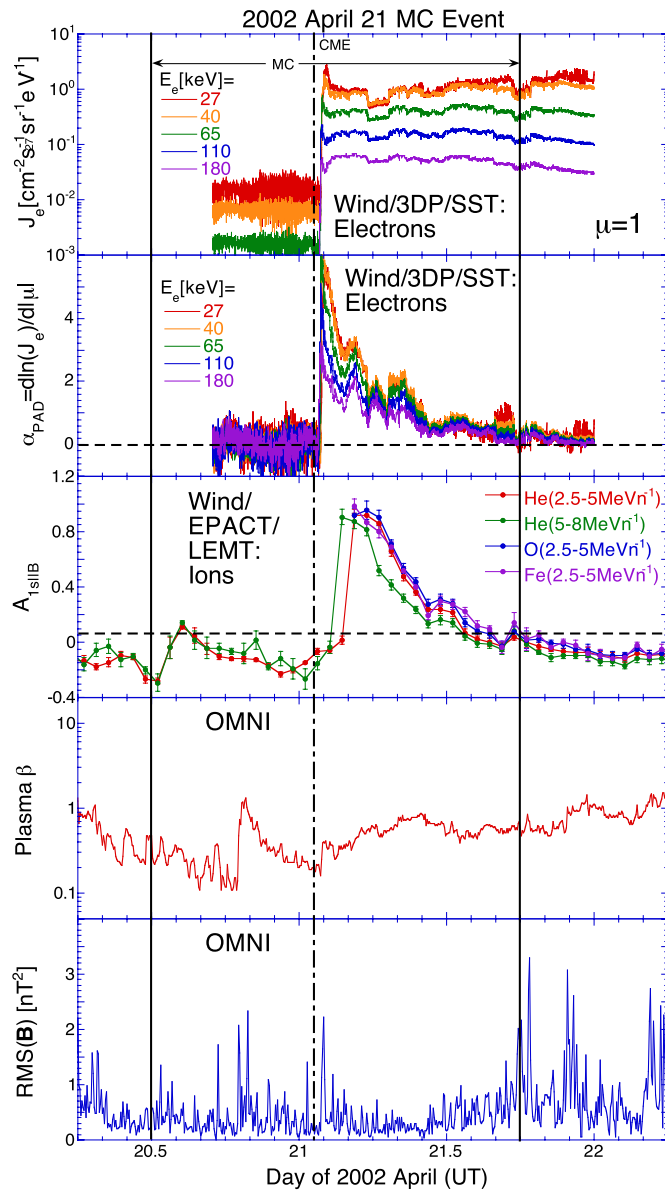


Figure 12. Same as Figure 11 but for the 2002 April 21 MC event. (A color version of this figure is available in the online journal.)

Prior to the onset of the two MC events, there existed an isotropic background electron intensity, leading to the difficulty in the identification of α_{PAD} variations near the front boundary of MCs. Inside MCs, as time passes, α_{PAD} gradually decreases but with significant magnitude fluctuations. At the rear boundary α_{PAD} is close to zero for all electron energy channels examined. In addition, the $A_{1s||B}$ values of He, O, and Fe ions are also close to zero when both the front and rear boundaries are crossed. The finding that $\alpha_{\text{PAD}} \sim 0$ for SST electrons and $A_{1s||B} \sim 0$ for LEMT heavy ions implies that the magnetic field in the vicinity of the MC boundary is strongly turbulent.

We then examine the time profiles of plasma β and $\text{RMS}(\mathbf{B})$ in the exterior region of MCs. It can be seen that around the front boundary of MCs there exist a gradient of β and an enhancement of $\text{RMS}(\mathbf{B})$, which could affect particle scattering through the following processes.

1. According to Burlaga (1991), the gradient of β at the MC boundary should produce a ballooning instability (Strauss

1989), which could cause the transport of turbulence, leading to a broadened boundary layer with strong turbulence. While this mechanism has not been investigated in detail, Burlaga et al. (2001) pointed out that there might be a broader, turbulent transition at the front boundary, and a tail or wake at the rear boundary.

2. Leamon et al. (1998) examined the anisotropy of IMF fluctuations inside MCs. They found that near the center of MCs magnetic fluctuations are more nearly transverse to the mean field than that in the open field line case. Also, the wave vector is oriented at larger angles relative to the mean field vector. Therefore, Smith et al. (1999) pointed out that the weak scattering inside MCs is not only caused by the decreased magnitude of magnetic fluctuations, but also due to the orientation of the wave vector that is especially ineffective at scattering particles. Since the extremely transverse magnetic fluctuations only show up in the center of MCs, the magnetic fluctuations near the MC boundary could scatter particles.

Therefore, there should be sufficient electron scattering existing in the exterior region of MCs to support the extrapolation of $\langle \mu_{\text{omax}} \rangle$ and L_{0eII} to higher $t_{\text{h}} - t_{\text{ll}}$ values in Figure 6, leading to a scenario that $\langle \mu_{\text{omax}} \rangle$ could be close to zero when $L_{0eII} > 3$ AU.

4. SUMMARY

In this work, we have examined the *Wind*/3DP/SST electron data and *Wind*/EPACT/LEMT ion data to investigate the properties of GLE events during solar cycle 23. Our main findings are as follows.

1. Under the $\text{SRT}_e = t_{\text{RB}}$ assumption with $\text{RB} = \text{II}$ or III , the deduced path length $L_{e\text{RB}}$ of electrons is found to increase with increasing E_e , indicating that at higher energies the first arriving electrons may not experience scatter-free transport.
2. The increasing rate of $L_{e\text{RB}}/L_{0e\text{RB}}$, where $L_{0e\text{RB}}$ is the $L_{e\text{RB}}$ value measured at the lowest energy of SST, is correlated with the pitch angle distribution (PAD) of peak electron intensities locally measured, with a higher rate corresponding to a broader PAD. The correlation implies that the broadening of electron PADs at larger $L_{0e\text{RB}}$ events is due to a stronger IP scattering experienced by electrons in the local environment ($r > 0.5$ AU).
3. For the GLE events examined the correlation between $L_{0e\text{RB}}$ and L_{0i} are quite good for both $\text{RB} = \text{II}$ and III . The linear correlation coefficient is $R \sim 0.99$, indicating that the probability of $L_{0e\text{RB}}$ and L_{0i} being uncorrelated is $P \sim 1 \times 10^{-7}$. However, based on the correlation examination it is impossible to differentiate between $\text{RB} = \text{II}$ and III because of the closeness of t_{II} and t_{III} . The weighted averaged $L_{0e\text{RB}} = (0.91 \pm 0.04) L_{0i}$ is deduced from both $\text{RB} = \text{II}$ and III .
4. The solar longitude distribution and IMF topology of the GLE events examined are in favor of the CME-driven shock acceleration origin of the non-relativistic electrons observed.
5. The velocity difference between faster electrons and slower ions provides a method to estimate the stability of magnetic flux tubes. From the GLE events examined the estimated maximum stable time of magnetic flux tubes is 4.8 hr.

We gratefully acknowledge data provided by the NASA/Space Physics Data Facility (SPDF)/CDAWeb and

Wind/3DP Data Center. Also, we thank K. Ogilvie, R. Lin, and A. Szabo for their support of this work, and the anonymous reviewer for his/her valuable comments. The presented work has received funding from the European Union Seventh Framework Programme (FP7/2007–2013) under grant agreement No. 263252 [COMESSEP]. Also, D.V.R. is supported in part by NASA grant NNX08AQ02G. C.K.N. is supported in part by NASA grant NNX09AU98G. L.W. is supported in part by NASA grant NNX08AE34G.

REFERENCES

- Berger, M. J., Seltzer, S. M., Chappell, S. E., Humphreys, J. C., & Motz, J. W. 1969, *NuclIM*, **69**, 181
- Bieber, J. W., Dröge, W., Evenson, P. A., et al. 2002, *ApJ*, **567**, 622
- Bougeret, J.-L., Kaiser, M. L., Kellogg, P. J., et al. 1995, *SSRv*, **71**, 231
- Burlaga, L. F. 1991, in *Physics and Chemistry in Space: Space and Solar Physics*, Vol. 21, *Physics of the Inner Heliosphere II*, ed. R. Schwenn & E. Marsch (Berlin: Springer), 1
- Burlaga, L. F., Skoug, R. M., Smith, C. W., et al. 2001, *JGR*, **106**, 20957
- Cane, H. V. 2003, *ApJ*, **598**, 1403
- Cane, H. V., Richardson, I. G., & von Rosenvinge, T. T. 2010, *JGR*, **115**, A08101
- Chollet, E. E., & Giacalone, J. 2011, *ApJ*, **728**, 64
- Cliwer, E. W. 2008, in *IAU Symp. 257, Universal Heliophysical Processes*, ed. N. Gopalswamy & D. F. Webb (Cambridge: Cambridge Univ. Press), 401
- Ganse, U., Kilian, P., Vainio, R., & Spanier, F. 2012, *SoPh*, **280**, 551
- Gopalswamy, N., Xie, H., Yashiro, S., et al. 2012, *SSRv*, **171**, 23
- Gosling, J. T., Skoug, R. M., & McComas, D. J. 2003, *GeoRL*, **30**, 1967
- Graham, D. B., Cairns, I. H., Malaspina, D. M., & Ergun, R. E. 2012, *ApJL*, **753**, L18
- Haggerty, D. K., & Roelof, E. C. 2002, *ApJ*, **579**, 841
- Haggerty, D. K., Roelof, E. C., & Simnett, G. M. 2003, *AdSpR*, **32**, 2673
- He, H.-Q., & Wan, W. 2012, *ApJ*, **747**, 38
- He, H.-Q., Qin, G., & Zhang, M. 2011, *ApJ*, **734**, 74
- Jokipii, J. R. 1971, *RvGeo*, **9**, 27
- Jokipii, J. R., & Parker, E. N. 1969, *ApJ*, **155**, 777
- Kahler, S. W. 2007, *SSRv*, **129**, 359
- Kahler, S. W., Aurass, H., Mann, G., & Klassen, A. 2007, *ApJ*, **656**, 567
- Kahler, S. W., Haggerty, D. K., & Richardson, I. G. 2011a, *ApJ*, **736**, 106
- Kahler, S. W., Krucker, S., & Szabo, A. 2011b, *JGR*, **116**, A01104
- Kahler, S. W., & Ragot, B. R. 2006, *ApJ*, **646**, 634
- Kocharov, L., Saloniemi, O., Torsti, J., Kovaltsov, G., & Riihonen, E. 2007, *ApJ*, **654**, 1121
- Krucker, S., Kontar, E. P., Christe, S., & Lin, R. P. 2007, *ApJL*, **663**, L109
- Krucker, S., Larson, D. E., Lin, R. P., & Thompson, B. J. 1999, *ApJ*, **519**, 864
- Kundu, M. R. 1965, *Solar Radio Astronomy* (New York: Wiley-Interscience)
- Larson, D. E., Lin, R. P., McTiernan, J. M., et al. 1997, *GeoRL*, **24**, 1911
- Leamon, R. J., Smith, C. W., & Ness, N. F. 1998, *JGR*, **25**, 2505
- Lin, R. P. 1974, *SSRv*, **16**, 189
- Lin, R. P. 1985, *SoPh*, **100**, 537
- Lin, R. P., Anderson, K. A., Ashford, S., et al. 1995, *SSRv*, **71**, 125
- Matthaeus, W. H., Dasso, S., Weyand, J. M., et al. 2005, *PhRvL*, **95**, 231101
- Mazur, J. E., Mason, G. M., Dwyer, J. R., et al. 2000, *ApJL*, **532**, L79
- Mewaldt, R. A., Cohen, C. M. S., Haggerty, D. K., et al. 2003, in *Proc. 28th Int. Cosmic Ray Conf.*, Vol. 6, ed. T. Kajta, Y. Asaoka, A. Kawachi et al. (Tokyo: Universal Academy Press, Inc.), 3313
- Ng, C. K., Reames, D. V., & Tylka, A. J. 2003, *ApJ*, **591**, 461
- Nitta, N. V., Reames, D. V., De Rosa, M. L., et al. 2006, *ApJ*, **650**, 438
- Parker, E. N. 1963, *Interplanetary Dynamical Process* (New York: Wiley-Interscience)
- Reames, D. V. 1999, *SSRv*, **90**, 413
- Reames, D. V. 2002, *ApJL*, **571**, L63
- Reames, D. V. 2009a, *ApJ*, **693**, 812
- Reames, D. V. 2009b, *ApJ*, **706**, 844
- Reames, D. V. 2013, *SSRv*
- Richardson, J. D., Dashevskiy, F., & Paylarena, K. I. 1998, *JGR*, **103**, 14,619
- Richardson, J. D., & Paularena, K. I. 2001, *JGR*, **106**, 239
- Rouillard, A. P., Sheeley, Jr., N. R., Tylka, A., et al. 2012, *ApJ*, **752**, 44
- Saiz, A., Evenson, P., Ruffolo, D., & Bieber, J. W. 2005, *ApJ*, **626**, 1131
- Smith, C. W., Leamon, R. J., Ness, N. F., et al. 1999, in *Proc. 26th Int. Cosmic Ray Conf.*, ed. by D. Kieda, M. Salamon, & B. Dingus (Salt Lake City, UT: Univ. of Utah), 7, 4809
- Strauss, H. R. 1989, *GeoRL*, **16**, 219
- Tan, L. C., Malandraki, O. E., Reames, D. V., et al. 2012, *ApJ*, **750**, 146
- Tan, L. C., Mason, G. M., Lee, M. A., et al. 1992, *JGR*, **97**, 1597
- Tan, L. C., Reames, D. V., & Ng, C. K. 2007, *ApJ*, **661**, 1297
- Tan, L. C., Reames, D. V., Ng, C. K., Saloniemi, O., & Wang, L. 2009, *ApJ*, **701**, 1753
- Tan, L. C., Reames, D. V., Ng, C. K., Shao, X., & Wang, L. 2011, *ApJ*, **728**, 133
- Thejappa, G., MacDowall, R. J., Bergamo, M., & Papadopoulos, K. 2012, *ApJL*, **747**, L1
- Torsti, J., Riihonen, E., & Kocharov, L. 2004, *ApJL*, **600**, L83
- Turner, R. E. 2006, in *Solar Eruptions and Energetic Particles*, ed. N. Gopalswamy et al. (Geophys. Monogr. Ser., Vol. 165; Washington, DC: AGU), 367
- Tylka, A. J., Cohen, C. M. S., Diertrich, W. F., et al. 2003, in *Proc. 28th Int. Cosmic Ray Conf.*, Vol. 6, ed. T. Kajta, Y. Asaoka, A. Kawachi et al. (Tokyo: Universal Academy Press, Inc.), 3305
- Tylka, A. J., & Lee, M. A. 2006, *ApJ*, **646**, 1319
- Tylka, A. J., Malandraki, O. E., Dorrian, G., et al. 2012, *SoPh*
- von Rosenvinge, T. T., Barbier, L. M., Karsch, J., et al. 1995, *SSRv*, **71**, 155
- Wang, L., Lin, R. P., & Krucker, S. 2011, *ApJ*, **727**, 121
- Wang, L., Lin, R. P., Krucker, S., & Gosling, J. T. 2006, *GeoRL*, **33**, L03106
- Wiedenbeck, M. E., Mason, G. M., Cohen, C. M. S., et al. 2011, in *Proc. 32nd Int. Cosmic Ray Conf.*, Vol. 10, ed. Y. Tan et al. (Beijing: Institute of High-Energy Physics), 10, 205
- Wild, J. P., Smerd, S. F., & Weiss, A. A. 1963, *ARA&A*, **1**, 291